# Controls on Solubility and Deposition of Quartz, Calcite, Fluorite and Anhydrite in Boiling Saline Hydrothermal Systems

by

Jackson Barrier

A thesis submitted in partial fulfillment of the requirements of the degree of

Master of Science

Department of Earth and Atmospheric Sciences

University of Alberta

# Abstract

Fluid boiling is a key mechanism for precipitation of minerals in epithermal deposits, and evidence for boiling includes a variety of vein mineral textures that indicate rapid deposition. Hence, the relationships between vein mineral paragenesis and boiling are critical to interpreting processes that drive mineralization. Here, we evaluate quantitatively the factors that control solubility and deposition of four common epithermal vein minerals – quartz, calcite, fluorite and anhydrite – in boiling hydrothermal fluids ranging from 0 to 15 wt% NaCl. Major controls on the precipitation of these minerals include the initial salinity of fluid; the temperature at which boiling commences; the extent of vaporization; and magnitude of temperature decrease during progressive boiling. At 0 wt% NaCl, solubilities of all four minerals in the liquid phase increase with increasing temperature up to a local maximum (336 °C for quartz; 287 °C for calcite; 300 °C for fluorite; and 100 °C for anhydrite). Solubility of each mineral in the liquid phase decreases with increasing temperature thereafter (a phenomenon referred to as retrograde solubility), and converges with that in the vapor phase at the critical point of $H_2O$. As fluid salinity increases, solubilities of all four minerals increase, but to different extents. Specifically, the solubilities of calcite, fluorite and anhydrite show strong salting-in effects in comparison to that of quartz. For quartz, calcite, and fluorite, salting-in eventually overcomes the retrograde solubility trends, such that the temperature dependence of solubility is strictly prograde at salinities exceeding a certain threshold (approximately 6 wt% NaCl for quartz; 3 wt% NaCl for calcite; 1 wt% NaCl for fluorite). Anhydrite stands apart in that it exhibits a strictly retrograde trend for all salinities up to 10 wt% NaCl, and only sees a limited prograde trend at temperatures close to the critical point for a fluid of 15 wt% NaCl. The various factors affecting boiling-induced deposition of all three minerals allow for a variety of distinct paragenetic sequences

depending on fluid salinity, temperature and extent of vaporization and cooling. Our results provide a framework for both qualitative and quantitative interpretations of vein paragenesis and relationships between fluid composition, boiling and mineral deposition.

# Preface

Chapters 1-4 have been submitted to Mineralium Deposita, co-authored by myself and Matthew Steele-MacInnis. I was responsible for conducting the analysis and composing the manuscript. Matthew Steele-MacInnis designed and supervised this thesis project and composed the paper.

## Acknowledgements

I would like to thank my supervisor Matthew Steele-MacInnis for his guidance and support over the past two year. He has taught me so much, and as an international student the pandemic created several complications, but with his help and advice, I will be able to finish on schedule. I am thankful to Pilar Lecumberri-Sanchez for sitting on my supervisory committee and for being a guide and teacher over the course of this project. I am grateful for Yury Klyukin and being able to use his modeling program for the thermodynamic properties of H2O-NaCl fluids, which facilitated so much of my research. I am appreciative that this research was funded by NSERC through a Discovery grant to Matthew Steele-MacInnis. I am grateful to Shane Scoggin, Adam Trzinksi, and Nathan Swaim for their encouragement throughout my graduate degree. Thank you to Ryann Schoene, as well as my friends and family, for all the love and support they provide to all my endeavours.

# Table of Contents

# List of Figures

# 1. Introduction

Fluid phase separation (commonly referred to as "boiling") is widely regarded as a key mechanism driving mineralization—and especially high-grade mineralization—in epithermal ore deposits. Boiling is a common phenomenon in these shallow hydrothermal systems, as documented by a variety of evidence including direct observation at fumaroles; fluid inclusions in veins; mineral textures; and experience with engineered systems such as geothermal wells (Chambefort and Stefánsson, 2020). The occurrence of boiling in these systems is governed by a variety of factors including pressure, temperature, and salinity of the fluid. In systems where fractures are open to the surface, once boiling commences it generally continues to the surface (Fournier, 1985; Vikre, 1985; Henley and Brown, 1985; Cline et al.,1992; Moncada et al., 2012). In this scenario, the depth interval at which boiling commences is referred to as the "boiling horizon," and precious metal mineralization is commonly richest either at or near the base of the boiling horizon (Moncada et al., 2012). Depending on the bulk enthalpy of the ascending fluid, only a small amount of the liquid phase may be converted to vapor during this process, which is therefore referred to as "gentle boiling" (Moncada et al., 2012). In contrast, "flashing" represents a near-instantaneous conversion of liquid water to steam driven by sudden drop in pressure, for example by tectonic movement (Brown, 1986; Weatherley and Henley, 2013). This latter mode of boiling can be responsible for especially rapid mineral deposition, which generates textures such as colloform quartz and bladed calcite (Moncada et al., 2012). Again, high-grade zones in epithermal deposits commonly correlate with the boiling horizon (Buchanan, 1981; Cline et al., 1992; Hedenquist et al., 2000), but the correlation varies somewhat depending on whether fluids underwent gentle boiling or flashing. In cases of gentle boiling, precious metal mineralization is generally most concentrated at depths slightly shallower than the base of the boiling horizon. In

the case of flashing, highest grades tend to be concentrated right at the base of the boiling horizon (Simmons and Browne, 2000).

Mineral textures are commonly amongst the best diagnostic features for distinguishing minerals that were deposited by boiling. In general, "boiling textures" are those that indicate rapid deposition, including for example amorphous forms (deposition rate exceeding the timescale necessary to form structured crystals); very fine grain sizes (nucleation rate exceeding the rate at which solutes can diffuse to the growing crystal faces); and skeletal/hopper-type forms (preferential growth along certain crystallographic axes; Moncada et al., 2012). Common boiling textures among epithermal vein minerals include plumose or "feathery" quartz; colloform-textured silica/quartz (Fig. 1A); bladed calcite; and bladed calcite replaced by quartz (Fig. 1A; Roedder, 1984; Bodnar et al., 1985; Fournier, 1985; Simmons and Christenson, 1994; Dong et al. 1995; Henley and Hughes, 2000; Moncada et al., 2012; Zeeck et al., 2021)). Quartz exhibits a variety of boiling textures in both low- and high-sulfidation epithermal veins. Bladed calcite (±replaced by quartz) is common in low-sulfidation settings but absent from high-sulfidation systems due to their lower pH (White and Hedenquist, 1995; Hedenquist and Arribas, 2017; Hedenquist and Arribas, 2022). The particular case of bladed calcite replaced by quartz (Fig. 1A) is a common feature in low-sulfidation epithermal veins, and suggests that calcite was first rapidly deposited, then gradually re-dissolved concurrently with deposition of quartz. High sulfidation veins also commonly host anhydrite, which is absent from low-sulfidation veins (Klimentyeva et al., 2021; Hedenquist and Arribas, 2022). Meanwhile, gold telluride (Au-Te) type epithermal systems associated with alkalic magmatism commonly host abundant fluorite in veins along with quartz and calcite (Fig. 1B; Jensen and Barton, 2000). In sum, a variety of vein mineral assemblages and paragenetic sequences have been described in epithermal systems of

different types, which likely reflect different ore-forming fluid properties and fluid evolution. The main focus of this study is to explore some of the factors that may govern these variations through numerical modeling of mineral solubility.

By thermodynamic modeling of the solubility of quartz in a pure-$H_2O$ fluid, Cline et al. (1992) showed that fluid boiling is an effective mechanism for deposition of quartz in epithermal veins. This is largely because the solubilities of minerals in hydrothermal fluids are strongly dependent on fluid density (Akinfiev and Diamond, 2009; Dolejs and Manning, 2010; Brooks and Steele-MacInnis, 2019; Steele-MacInnis and Manning, 2020; Creaser et al., 2021). When boiling occurs, the initially single-phase fluid separates into a higher density liquid and a lower density vapor, and the proportion of vapor increases as boiling proceeds. Because of the strong correlation between density and solubility, the solubility of any given mineral is inevitably higher in the liquid phase and lower in the vapor. Hence, as the proportion of vapor increases, the bulk (total) solubility of the mineral declines, resulting in precipitation. When flashing occurs, this decrease in solubility may be especially abrupt and precipitous, resulting in especially rapid deposition of vein minerals. By numerical modeling, Cline et al. (1992) showed that quartz precipitation in systems involving pure $H_2O$ is dependent on the temperature at which boiling commences, the rate that the fluid temperature decreases, and the extent of fluid vaporization.

In the present study, we build upon the earlier work of Cline et al. (1992) and extend this approach to saline fluids, as well as to a variety of common gangue minerals in addition to quartz. Specifically, we apply new thermodynamic models for the solubilities of quartz, calcite, fluorite and anhydrite in $H_2O$-NaCl fluids to investigate the factors that affect the transport of solutes and deposition of these minerals.

## 2. Methods

We modeled the solubility of quartz, calcite, fluorite and anhydrite under conditions of fluid boiling in the system $H_2O$-NaCl, for bulk compositions ranging from 0-15 wt% NaCl and for temperatures ranging from 100 °C to the respective critical points (up to 374 °C for pure $H_2O$, and up to ~500 °C for a fluid of 15 wt% NaCl; Fig. 2). The range of fluid salinities was selected based on the data synthesis presented by Bodnar et al. (2014) and Steele-MacInnis et al. (2021). The range of temperatures was selected in part based on the fluid phase equilibria (i.e., the critical temperatures) but also overlaps well with the known range of temperatures of epithermal systems (see Bodnar et al., 2014). Specifically, epithermal mineral deposits were first defined by Lindgren (1907) as having a shallow depth and a temperature range of 50-150 °C, but Lindgren (1933) later increased the upper limit to 200 °C, and epithermal deposits are now generally considered as the shallow expressions of larger hydrothermal systems that extend up to temperatures of at least 300 °C and depths <1.5km (Gemmell and Simmons, 2007). Some workers have also reported significantly higher fluid temperatures in some high-sulfidation deposits up to >450°C (Hedenquist and Lowenstern, 1994; Mavrogenes et al., 2010).

We modeled the fluid phase equilibria using a modified version of the computer program of Klyukin et al. (2020). This program implements the IAPWS-95 formulation equation state of Wagner and Pruß (2002) for pure $H_2O$; the model of Driesner and Heinrich (2007) for the phase equilibria of $H_2O$-NaCl fluids; and the model of Driesner (2007) for the densities and enthalpies of $H_2O$-NaCl fluids (Driesner, 2007). Solubilities of quartz, calcite, and fluorite were calculated using the model of Brooks and Steele-MacInnis (2019), and that of anhydrite was calculated using the model of Creaser et al. (2022). We modified the program of Klyukin et al. (2020) to enable calculation of isenthalpic cooling paths, by adding an iterative solver to adjust pressure at

each step along the cooling path such that bulk enthalpy was conserved. We also added tools to back-calculate microthermometric properties and room-temperature volume fractions of phases in fluid inclusions representative of fluids trapped at various points along the cooling or decompression paths.

## 3. Results

### 3.1 Fluid Phase Equilibria

In the $H_2O$ system, the liquid-vapor curve is a univariant element that terminates at the critical point at approximately 374 °C and 22 MPa (Fig. 2A). Consequently, boiling in this system is limited to temperatures less than 374 °C; the pressure at which boiling occurs is uniquely defined as a direct function of temperature; and both density and specific enthalpy (as well as solubilities of minerals) in both liquid and vapor are also uniquely defined as functions of temperature under conditions of boiling (Fig. 3). Hence, calculations of bulk (total) mineral solubility during boiling in this system is relatively straightforward because the only sliding variable at any given temperature and pressure along the liquid-vapor curve is the relative mass fraction of liquid versus vapor, which is itself a direct function of the bulk enthalpy of the system (Fig. 3A).

In the case of $H_2O$-NaCl fluids, the situation is somewhat more complicated owing to the added degree of freedom, such that for a given bulk salinity and temperature, boiling can occur over a range of pressures, bounded at lower pressures by the liquid-vapor-halite curve (which separates a low-pressure field of vapor+halite from that of liquid+vapor) and at higher pressures by the critical curve (which separates the liquid+vapor field from that of single-phase fluid; Fig. 2). Hence, the compositions, densities and specific enthalpies (as well as solubilities of minerals)

of both liquid and vapor vary across this range. To overcome this added complexity and allow for straightforward visualization of the results in two-dimensional graphs (Figs. 3-7), we adopted the following conventions: For each studied salinity, we held the salinity of the *liquid* phase constant at the set value, and calculated the composition of vapor in equilibrium with a liquid of that salinity. Hence, Figs. 3-7 effectively show the variation of fluid properties and mineral solubilities along the bubble-point curve for each given salinity, and the salinity of the corresponding (conjugate) vapor is a sliding variable along each plotted curve (ranging from ~0 at 100 °C, up to the same salinity as the liquid phase as the two curves converge at the critical point).

For a pure $H_2O$ fluid, the enthalpy of the liquid increases and liquid density deceases as temperature approaches the critical point (Fig. 3A). In the vapor phase, enthalpy increases slightly as temperatures rises from 100 °C before decreasing to meet the liquid phase at the critical point. The density of the vapor remains low until temperature exceeds ~300 °C, whereupon density begins to increase sharply towards the critical point (Fig. 3B). As the salinity of the liquid phase increases, both the enthalpies and densities at the critical point increases. As salinity of that liquid is increased, the temperature dependence of both the density and specific enthalpy of conjugate vapor begins to flatten at high temperatures, such that the critical point does not impart such strong variations in physical properties for saline fluids it does for pure $H_2O$ (Fig. 3; Klyukin et al., 2016).

### 3.2 Quartz

For a fluid of pure $H_2O$ along the liquid-vapor curve, the solubility of quartz in the liquid phase increases consistently as temperature increases from 100 up to ~336 °C. At 336 °C, the solubility of quartz in the liquid phase reaches a local maximum, and begins to decrease with

increasing temperature thereafter to converge with the lower solubility of quartz in the vapor phase at the critical point of $H_2O$ (Fig. 4A). Quartz solubility in the vapor phase is mostly negligible from 100 to ~350°C and increases strongly thereafter to converge with that in the liquid phase at the critical point (Fig. 4A). As salinity increases, the solubility of quartz in the liquid phase at any given temperature increases (Fig. 5A). Moreover, the retrograde trend of quartz solubility in the liquid observed at 0 wt% NaCl is gradually diminished until the trend in solubility in the liquid becomes strictly prograde at salinities > 6 wt% NaCl (Fig. 5A).

### 3.3 Calcite

Calcite is much less soluble than quartz in a pure $H_2O$ fluid, especially so in the vapor phase and at the critical point where solubility of calcite is negligible (Fig. 4B). Notably, the local maximum of calcite solubility and the subsequent retrograde trend of calcite solubility in the liquid phase are both shifted to lower temperatures compared to quartz, starting at ~287°C (Fig. 4B). The solubility of calcite in the liquid phase is also much more strongly dependent on fluid salinity compared to quartz (Fig. 5B). For example, in a saline fluid of 15wt% NaCl, calcite solubility reaches values more than 100x greater than in pure $H_2O$. This latter strong salting-in was discussed in detail by Brooks and Steele-MacInnis (2019), who showed that the salting-in for calcite is driven primarily by the formation of sodium and/or chloride complexes in aqueous solution. Moreover, while calcite solubility in the liquid phase increases with increasing salinity, the solubility in the vapor phase increases even more so, such that solubility of calcite at the respective critical points varies from essentially negligible in pure $H_2O$ up to values commensurate with that in the liquid phase for saline fluids (Fig. 5B). The retrograde trend of

solubility in the liquid phase also vanishes for salinities >2wt% NaCl (Fig. 5B), such that the trend in solubility becomes strictly prograde.

### 3.4 Fluorite

Of the minerals investigated here, fluorite has the lowest solubility in pure $H_2O$ (Fig. 4C), but also the strongest degree of salting-in (Fig. 5C). Like quartz and calcite, fluorite displays a retrograde trend in solubility in the liquid phase, with the local maximum in solubility in pure $H_2O$ occurring at ~300°C. Like that of calcite, fluorite solubility in the vapor phase of pure $H_2O$ is negligible at all temperatures from 100 °C through to the critical point (Fig. 4C). Solubility of fluorite in the liquid phase increases dramatically with increasing salinity, with the maximum solubility at 15 wt% NaCl more than 500x greater than the maximum solubility in pure $H_2O$ (Fig. 5C). This very strong salting-in was discussed by Creaser et al. (2021) as reflecting the formation of sodium and/or chloride complexes in solution, similar to the case for calcite. Also similar to the case for calcite, the retrograde solubility of fluorite ceases as salinity increases, such that the trend in solubility in the liquid phase is strictly prograde at >2wt% NaCl (Fig. 5C).

### 3.5 Anhydrite

Anhydrite solubility trends are distinctly different from the other gangue minerals studied here, in that the solubility of anhydrite shows a mostly retrograde temperature dependence across nearly the whole range of temperatures and salinities studied here (Figs. 4D and 5D). Hence, the solubility of anhydrite is significantly higher than that of the other three minerals at 100 °C. The solubility in the liquid phase decreases rapidly as temperature increases, dropping nearly to zero

mmol/kg by 300 °C. The solubility of anhydrite in the vapor phase in pure $H_2O$ fluids is negligible from 100 °C through to the critical point.

Anhydrite solubility has a higher dependance on the salinity of the fluid than quartz, but less so than fluorite and calcite. For example, in a saline fluid of 15 wt% NaCl, the maximum solubility of anhydrite is ~5x greater than that in pure $H_2O$ (*c.f.* 100x for calcite, and 500x for fluorite). Also, in the case of anhydrite, while increasing salinity leads to modest salting-in, this salting-in is insufficient to overcome the overall retrograde trend in solubility, such that the trend is solubility is still mostly retrograde even at 15 wt% NaCl. Only at 15 wt% NaCl, the solubility shows a limited range of prograde behavior, and only at temperatures close to the critical point (Fig. 5D).

**3.6 Pathways to mineral precipitation**

Cline et al. (1992) discussed quartz deposition along different fluid pressure temperature paths, which can be broadly broken down into two end member paths: a cooling path in which the pressure-temperature conditions follow the slope of the liquid-vapor curve (i.e., representative of gentle boiling); and an isothermal decompression path (which in the case of pure $H_2O$, leads to an abrupt phase transition from liquid to vapor, i.e. flashing). Here, we take a similar approach, and we introduce two calculated parameters that aid in quantifying the degree to which each type of pathway contributes to mineral precipitation. Firstly, for the case of the gentle boiling path along the liquid-vapor curve, we compute the $\delta$solubility/$\delta$temperature slopes, which quantify how solubility of a mineral in the liquid phase changes as a function of temperature along the boiling curve (Fig. 6). Secondly, we compute the absolute difference ($\Delta$) in solubility between liquid and conjugate vapor along the boiling curve, which quantifies the amount of mineral deposited per aliquot of liquid converted to vapor (Fig. 7). In real

hydrothermal systems, mineral deposition will generally be driven by both of these factors concomitantly as cooling, ascent and boiling proceed. Nevertheless, subdividing the two mechanisms this way is useful in order to disentangle especially the different degrees to which simple cooling versus vaporization affect mineral deposition.

For a pathway that follows the liquid-vapor curve during gentle boiling and cooling, mineral precipitation will take place only if the $\delta$solubility/$\delta$temperature term is positive (i.e., prograde temperature dependence of solubility), and the extent to which a certain mineral is expected to precipitate correlates with the magnitude of this term (Fig. 6).

Quartz precipitation by gentle boiling is therefore permitted up to a certain threshold temperature for all salinities from 0 to 6 wt% NaCl, and over the full range of temperature up to the critical point for fluids of ≥8 wt% NaCl (Fig. 6A). However, low-salinity fluids from 0 to 6 wt% NaCl will generally *not* deposit quartz by gentle boiling alone above the threshold temperature of the local maximum of solubility (336 °C at 0 wt% NaCl, and increasing with increasing salinity; Fig. 6A). The magnitude of $\delta$solubility/$\delta$temperature for quartz is optimized for almost the whole range of studied salinities in the vicinity of 300 °C, implying that quartz precipitation is expected to be most intense during cooling along the liquid-vapor curve in this temperature range irregardless of salinity (Fig. 6A). However, this window of optimal $\delta$solubility/$\delta$temperature for quartz precipitation extends out to higher temperatures >400 °C for the more saline fluids of 8, 10 and 15 wt%, implying that quartz precipitation can proceed through the porphyry-to-epithermal transition for fluids of moderate salinity.

Calcite and fluorite display similar trends in Fig. 6 and therefore these trends are described together here. For fluids of low salinity of 0 to 2 wt% NaCl, the $\delta$solubility/$\delta$temperature term for both calcite and fluorite is either mostly negative or around

zero, implying that gentle boiling along the liquid-vapor curve is an ineffective mechanism to deposit these minerals (Fig. 6B, C). Similarly, for all salinities studied here, these two minerals show negligible $\delta$solubility/$\delta$temperature at temperatures <200 °C, implying that these minerals are unlikely to precipitate by gentle boiling at low temperatures. However, with increasing temperature and especially salinity ≥4 wt% NaCl, the $\delta$solubility/$\delta$temperature term for calcite and fluorite increase significantly, such that these minerals can be precipitated readily by gentle boiling of moderately saline fluids above 200 °C. Precipitation of these minerals by gentle boiling is expected to be most intense for fluids of highest salinity, and especially at higher temperatures approaching the respective critical points (Fig. 6B, C).

Anhydrite shows a quite distinct pattern of $\delta$solubility/$\delta$temperature compared to all three other minerals, with mostly negative values across nearly the whole range of studied temperatures and salinities (Fig. 6D). This means that gentle boiling and cooling along the liquid-vapor curve is virtually never an effective mechanism to precipitate anhydrite, and in fact any preexisting anhydrite in the rock might be expected to dissolve as the ascending fluid cools. Only in the case of a fluid of 15 wt% NaCl-$H_2O$, the $\delta$solubility/$\delta$temperature slope of anhydrite is positive and only above ~450°C. As this high salinity fluid cools along the liquid-vapor curve from higher temperatures, anhydrite would be able to precipitate over a narrow temperature range, but this would cease mineralization as the fluid cooled to temperatures below ~450 °C.

In the case of an isothermal decompression path and conversion of liquid water to steam, the $\Delta$solubility term (that in the liquid, minus that in the conjugate vapor) is always positive over the whole range of temperatures and salinities studied here. In other words, conversion of liquid water to steam inevitably leads to a decrease in solubility, driving mineral precipitation.

However, the conditions at which such flashing-induced deposition is optimized depend on a number of factors.

For quartz, the Δsolubility term is essentially identical for all salinities up to ~300 °C, implying that deposition of quartz by flashing will be nearly the same up to 300 °C irrespective of salinity (Fig. 7A). With increasing salinity, the maximum value of Δsolubility for quartz increases and shifts to higher temperatures, implying that more saline fluids are capable of depositing more quartz by flashing and at higher temperatures. However, for fluids of all salinities, as temperature approaches the critical point, the value of Δsolubility decreases precipitously to zero at the critical point (where solubility of quartz in the liquid is by definition the same as that in the vapor; Fig. 7A), such that flashing at near-critical conditions is ineffective for quartz deposition. The latter is a natural consequence of the nature of the critical point, and indeed holds true for calcite, fluorite and anhydrite as well.

Calcite and fluorite again show very similar trends in Δsolubility (Fig. 7B and C)and are discussed together. Both minerals show negligible values of Δsolubility up to ~225 °C for all salinities (Fig. 7B and C), implying that flashing at low temperatures is not an effective means to precipitate calcite or fluorite. At higher temperatures, the Δsolubility term remains low for fluids of 0 and 2 wt% NaCl, such that flashing of such low salinity fluids is also not very effective for depositing these minerals. In contrast, for fluids of higher salinity (and especially at the highest salinities of 8, 10 and 15 wt% NaCl), the Δsolubility term for both calcite and fluorite reaches high values, particularly at temperatures >300 °C, such that flashing-induced deposition of calcite and fluorite are highly efficient for moderately saline fluids at such temperatures (Fig. 7B and C).

Anhydrite once again stands apart in terms of trends in Δsolubility compared to the other minerals (Fig. 7D). For all salinities studied here, the maximum values of Δsolubility are attained at the lowest temperature of 100 °C, on account of the strongly retrograde solubility trends in the liquid phase. This implies that, distinct from the other three minerals, anhydrite will be deposited most efficiently by flashing at the lowest temperatures considered here – essentially, in the very near surface environment. Moreover, for the lowest salinity fluids of 0 and 2 wt% NaCl, the Δsolubility term for anhydrite declines to negligible values with increasing temperature >200 °C (Fig. 7D), implying that flashing of low-salinity fluids at high temperatures is an ineffective mechanism for anhydrite deposition. Fluids of higher salinity similarly show only declining Δsolubility for anhydrite as temperature is increased, but Δsolubility still retains modest values up to close to the respective critical points, implying that flashing at higher temperatures is less effective for anhydrite deposition, but some amount of anhydrite deposition is still permissible so long as the starting fluid salinity is higher.

## 4. Discussion

### 4.1 Controls on mineral solubility

Salinity is a major control on mineral solubility and deposition (Steele-MacInnis et al., 2012a; Steele-MacInnis et al., 2012b; Monecke et al., 2018; Brooks and Steele-MacInnis, 2019; Creaser et al., 2021), and our results indicate that all four minerals studied here show salting-in, but to quite different extents. As salinity is increased from 0 to 15 wt% NaCl, the *maximum* solubility of fluorite increases by ~500x, whereas that of calcite increases by ~100x, that of anhydrite by ~5x, and that of quartz by only ~3x. If, instead of maximum solubility, we compare the solubilities of each mineral 0 to 15 wt% NaCl-$H_2O$ fluid at a fixed temperature of 300 °C,

quartz solubility barely increases, whereas calcite solubility increases by ~8x, that of fluorite increases by ~25x, and that of anhydrite increases by ~400x. The implication of these simple comparisons is that epithermal systems involving higher-salinity fluids are much more likely to contain more calcite, fluorite and possibly anhydrite in veins, owing to the potentially higher solute load of aqueous calcium fluoride, carbonate and sulfate. The latter may explain for example why epithermal Au-Te systems associated with alkaline magmatism commonly exhibit fluorite- and calcite-rich veins, because ore-forming fluids in such systems commonly show relatively high salinities up to or exceeding 15 wt% NaCl (Jensen and Barton, 2000; Chen et al., 2022). Another implication of the strong salting-in of fluorite, calcite and anhydrite is that gentle boiling of an $H_2O$-NaCl fluid of finite salinity may be less effective for depositing these minerals, compared to quartz. This is because during gentle boiling of an $H_2O$-NaCl fluid, the salinity of the liquid phase increases progressively, which can result in an increase in bulk solubility even though the mass fraction of liquid declines. The latter is explored quantitatively by numerical simulations, below.

Fluid temperature also exerts a strong influence on the solubilities of all four minerals, but in different ways depending on the mineral as well as on the salinity. In the case of pure $H_2O$, each mineral shows a different temperature of maximum solubility, with a prograde solubility trend at lower temperatures and a retrograde trend at higher temperatures up to the critical point. Consequently, if a fluid of pure $H_2O$ enters the epithermal environment at temperatures near the critical point cools thereafter (such as in the case of "supercritical" geothermal systems; Scott et al. 2015), the solubilities of all four minerals will initially *increase*, rendering mineral precipitation unlikely and even allowing for progressive dissolution of these minerals from the country rock or from previously deposited veins. However, as the fluid cools through the

temperature of maximum solubility, precipitation would be enabled, in the sequence of first quartz, then fluorite, and lastly calcite. The latter sequence is exactly what is commonly observed for example in Au-Te systems associated with alkaline magmatism (Chen et al., 2022), and similar to the sequence of early quartz followed by late calcite in low-sulfidation epithermal veins (where lack of fluorite probably indicates that the fluids do not contain sufficient fluoride to ever reach fluorite saturation). In contrast, because anhydrite solubility continues to increase with decreasing temperature all the way to 100 °C, anhydrite precipitation would not occur in this scenario.

In the case of saline fluids, temperature continues to exert a strong control over the solubilities of all four minerals, both shifting the temperature of maximum solubility, and even eliminating the retrograde temperature dependence of solubility in some cases. The various effects of different combinations of temperature and salinity allow for a variety of sequences of mineral precipitation (and, potentially, dissolution) that are explored in the simulations below. Moreover, increasing salinity has profound effects on the solubilities of calcite, fluorite and anhydrite in the vapor phase, largely as a result of salting-in. As a result, depending on the temperature and salinity of the fluid, the solubilities of all four minerals in the vapor phase can reach non-negligible values, which implies that flashing (instantaneous conversion of liquid to vapor) may be less effective for mineral deposition, particularly if both salinity and temperature are high. In the case of anhydrite, the most effective window to maximize deposition by flashing would be at lower temperatures where the solubility in the liquid is greatest and the vapor is negligible (Figs. 5, 7D).

### 4.2 Solubility gradients and mineral deposition during boiling and flashing

To explore mineral precipitation mechanisms and sequences we constructed simulations that represent end-member pathways of isothermal decompression (Fig. 8 & 9) and isenthalpic cooling (Fig. 10 & 11). For the isothermal decompression simulation, four fluids of different salinity were modeled during decompression from 10 MPa to 5 MPa at 300 °C. Figure 8 shows the results of decompression of a pure $H_2O$ fluid (Fig. 8A) and a 1 wt% NaCl-$H_2O$ fluid (Fig. 8B). In panel A, the pure $H_2O$ fluid starts as a liquid at point **a** and decompresses to cross the boiling curve at point **b**, where the mass fraction of vapor increases abruptly from 0 to 100 % (Fig. 8C; i.e., flashing). At this point, the solubility of each mineral drops to effectively 0 mmol/kg, and all solutes in the fluid precipitate together, instantaneously, to yield simultaneous deposition of quartz, calcite, fluorite and anhydrite (Figs. 8D-G).

When fluid salinity is increased by only a small amount to 1 wt% NaCl, the situation changes significantly compared to the simulation for a pure-$H_2O$ fluid (Figs. 8B, H-L). This rather significant change with only a small amount of NaCl added reflects the increased variance of the system, and hence the additional degree of freedom during boiling across a range of pressure (Fig. 8B). In panel B, the fluid of 1 wt% NaCl-$H_2O$ starts as a single-phase liquid at point **d**. As decompression occurs, the fluid crosses into the liquid+vapor *field* at point **e**, and eventually crosses the liquid+vapor+halite curve and passes into the vapor+halite field at point **f**. Notice that this implies that the boiling fluid (with an initial salinity of only 1 wt% NaCl) undergoes a progressive increase in salinity as decompression and boiling proceed, reaching halite saturation at point **f**. This phenomenon has been described by Simmons and Browne (1997) and Kodera et al. (2005) as "boiling to dryness." As the decompression path passes point **e**, the solubilities of quartz, calcite, and fluorite all begin to decrease, and precipitation occurs. Quartz precipitation is especially rapid in the immediate vicinity of point **e**, and then tapers off to

a slower rate of precipitation most of the way towards point **f**. In the case of calcite and fluorite, however, the solubility trend during decompression past point **e** rapidly reaches an inflection, such that the trend reverses and both calcite and fluorite show a progressive *increase* in solubility most of the way towards point **f**. This implies that calcite and fluorite, initially precipitated in the vicinity of point **e**, will be rapidly re-dissolved as decompression proceeds. This somewhat unintuitive increase in solubility of calcite and fluorite during decompression-induced boiling is a result of the strong salting-in of these minerals: As boiling proceeds and the salinity of the liquid phase increases, the solubilities of calcite and fluorite in the liquid phase also increase, and the salting-in is strong enough to overcome the declining mass fraction of liquid. Indeed, in the case of anhydrite, the salting-in effect precludes any precipitation from **e** to **f**. Only when the fluid reaches halite saturation and all remaining liquid is consumed at point **f** do calcite, fluorite and anhydrite finally undergo wholesale precipitation (along with the last residual silica in solution). Note that this point of precipitation by crossing the liquid-vapor-halite curve is the same for fluids of higher salinity (described below) because the starting salinity has no effect on the pressure-temperature conditions of the liquid-vapor-halite curve.

Figure 9 shows the results of isothermal decompression of higher-salinity fluids of 5 and 15 wt% NaCl-$H_2O$ fluid. These results are mostly similar to those described above for a fluid of 1 wt% NaCl (Fig. 8B) and only the few subtle differences are noted here. Firstly, as salinity increases, the increase of mass fraction of vapor during decompression becomes more gradual (Fig. 9C and H), which in turn leads to a smoother trend in the precipitation of quartz (Fig. 9D and I). Meanwhile, as the starting fluid salinity increases, the salting-in effects for calcite and fluorite are amplified such that fluorite precipitation during boiling is inhibited at both 5 and 15 wt% NaCl (Fig. 9F, K), while calcite only shows a small amount of precipitation that would be

rapidly re-dissolved at 5 wt% NaCl (Fig. 9E), and no precipitation during boiling at 15 wt% NaCl (Fig. 9J). Only when the decompression paths cross the liquid-vapor-halite curve are calcite, fluorite and anhydrite deposited (same as in the case of a bulk salinity of 1 wt% NaCl above).

In epithermal systems, ascending fluids commonly cool adiabatically during boiling (Henley et al. 1984; Anderson 2005). To model such a fluid pathway in pressure-temperature space, we conducted simulations of isenthalpic cooling wherein pressure was iteratively re-calculated at each increment of temperature decrease to maintain a constant bulk enthalpy. Figure 10 shows the results of our isenthalpic cooling simulations for fluids of pure $H_2O$ and 1 wt% NaCl-$H_2O$ fluid (inset in Fig. 10A shows the same path in temperature-enthalpy space). For the fluid of pure $H_2O$, we selected a starting specific enthalpy of the liquid of ~1500 kJ/kg on the liquid-vapor curve at point **a**. Because the fluid is of pure $H_2O$, the isenthalpic cooling pathway inevitably follows the univariant liquid-vapor curve exactly (Fig. 10A). As cooling proceeds, the mass fraction of vapor increases smoothly to maintain a constant bulk enthalpy (Fig. 10B), while the solubility of quartz consistently decreases driving steady quartz precipitation (Fig. 10C). As the fluid cools from point **a**, both calcite and fluorite initially show increasing solubility, on account of the retrograde temperature dependence of solubility at these conditions (Fig. 4B and C). However, with progressive cooling, both latter minerals eventually reach their solubility maxima, such that fluorite begins to precipitate at ~300 °C while calcite starts to precipitate at ~290 °C. In contrast, the solubility of anhydrite only increases along the entire isenthalpic cooling path (as well as the cooling paths for the other three modeled fluids discussed below).

The isenthalpic cooling simulation for a fluid of 1 wt% NaCl starting at point **b**, with a bulk enthalpy of ~2000 kJ/kg, mostly shows similar trends to the one for a pure-$H_2O$ fluid

described above, but with some subtle differences noted here. Firstly, owing to the chosen starting point, this simulation begins close to the relevant critical point (Fig. 10A). As a result of the anomalous curvature of the low-salinity dew-point curves (Bischoff and Pitzer, 1989) and anomalous variation of fluid properties near the critical curve (Klyukin et al., 2016), we observe that the mass fraction of vapor first increases sharply, then undergoes an inversion and decreases slightly, and then continues to increase steadily to 100 °C (Fig. 10G). These inversions in the mass fraction of vapor during the initial stages of isenthalpic cooling also result in an anomalous stage of quartz (re-)dissolution at temperatures of ~375 to 350 °C (Fig. 10H) . Calcite shows a trend of initially increasing solubility from point **b** to ~350°C followed by precipitation thereafter (similar to the case of the pure-$H_2O$ fluid), whereas fluorite shows only decreasing solubility, and anhydrite only increasing solubility, over the whole cooling pathway from point **b** to 100 °C (Fig. 10J, K). The simulations for starting salinities of 5 and 15 wt% NaCl show similar trends, only lacking the anomalous behavior imparted by the critical point for the 1 wt% NaCl simulation, and showing progressively smoother, more monotonoic increase in the mass fraction of vapor produced as bulk salinity increases (Fig. 11).

### 4.3 Vein textures, Paragenesis and Fluid Inclusions

Our analysis of the various pathways to mineral precipitation and our numerical simulations show that a number of different paragenetic sequences, including various scenarios of re-dissolution of previously deposited hydrothermal vein minerals, are possible depending on salinity, initial temperature and extent of vaporization. These results also allow us to make some predictions about the types of scenarios that can form certain observed mineral assemblages and paragenetic sequences. For example, Figure 1A shows a rather common vein texture from a low-sulfidation epithermal vein, in which early colloform-textured quartz gives way to bladed calcite,

which is then replaced by quartz (indicating re-dissolution of calcite simultaneous with quartz precipitation). Based on our results, we suggest that one potential scenario that can explain this paragenetic sequence is when a relatively dilute fluid of ~1 to 5 wt% NaCl underwent isothermal decompression. Such a scenario gives rise to all necessary factors to allow for the mineral assemblage, paragenetic sequence, and indeed textures seen in Fig. 1A: Firstly, quartz experiences especially rapid deposition immediately upon the fluid intersecting the liquid-vapor curve (Figs. 8I and 9D), allowing for formation of colloform quartz. Meanwhile, calcite first precipitates rapidly, allowing for the formation of bladed calcite, but then undergoes progressive re-dissolution (Figs. 8J and 9E) as quartz precipitation continues but slows to more gradual rates (Figs. 8I and 9D) allowing for pseudomorphic replacement to preserve the texture of the bladed calcite.

The vein shown in Figure 1B represents another example of a common epithermal texture that can be explained by our results, in this case one typical of an epithermal Au-Te deposit associated with alkalic magmatism (Chen et al., 2022). The vein in Fig. 1B shows a paragenetic sequence consisting of early quartz, followed by fluorite, and then lastly calcite. When compared to our simulations, this paragenesis could be deposited for example by a low salinity fluid experiencing gentle boiling along an isenthalpic cooling path. As seen in the simulation of the pure $H_2O$ fluid undergoing isenthalpic cooling (Fig. 10), precipitation begins with quartz, followed by fluorite, with calcite deposition being last. The latter sequence is principally controlled by the different temperatures of maximum solubility and retrograde versus prograde temperature dependence for these three minerals.

Our numerical simulations also allow us to predict quantitavely the expected microthermometric properties and room-temperature phase ratios of fluid inclusions that might

be trapped along each fluid pathway. It should be stressed that preservation of fluid inclusions in epithermal veins showing evidence of boiling is sometimes poor, for example because when amorphous silica is deposited and then recrystallizes to quartz, the primary fluid inclusions are likely destroyed (Bodnar et al., 1985; Sander and Black, 1988, Moncada et al., 2012). Nevertheless, fluid inclusions showing evidence of boiling are a common feature of epithermal veins and our results place some quantitative predictions on the types of inclusions that may be expected (Figs 8-13). For the isothermal decompression pathways, inclusions trapped at the highest pressures in the single-phase (liquid) field are represented by assemblages of only liquid-rich inclusions that homogenize to the liquid phase (Fig. 12, top). As pressure decreases and the fluid crosses the liquid-vapor curve to enter the liquid+vapor field, bimodal assemblages of coeval liquid-rich and vapor-rich inclusions are produced (Fig. 12, middle). Notice that, in the case of isothermal decompression pathways at an equal set temperature, the volumetric phase proportions and microthermometric properties of both liquid-rich and vapor-rich inclusions are independent of the bulk salinity of the system, such that the types and properties of inclusions observed in this scenario depend only on pressure and temperature (Fig. 12). This reflects the fact that compositions and densities of liquid and vapor are uniquely defined at any given pressure and temperature during liquid-vapor phase separation in a two-component system, in accordance with Gibbs' Phase Rule. Also noteworthy is that as decompression proceeds, the salinity of the liquid phase increases progressively, eventually reaching values high enough to generate brine inclusions that contain halite daughter minerals at room temperature (Fig. 12, inclusions trapped at 63 bar). The latter is true even in the case of simulations with a relatively dilute bulk salinity of even 1 wt% NaCl. The latter is consistent with the process of "boiling to dryness" of an ascending hydrothermal fluid, as interpreted by Simmons and Browne (1997) and

Kodera et al. (2005). When pressure is decreased further such that the fluid intersects and crosses the liquid-vapor-halite curve, all remaining liquid is finally consumed and assemblages of only vapor-rich inclusions can be produced (Fig. 12, bottom). Assemblages of this type would generally be interpreted as evidence of flashing, and notice that the volume fraction of liquid in such inclusions is so vanishingly small that the thin film of liquid may be commonly not optically detectable in inclusions of this type.

Figure 13 shows an array of different inclusions types that can be produced during gentle boiling along an isenthalpic cooling path for fluids of different salinities. The results in terms of room-temperature volume fractions share many similarities across the different salinities and pathways studied here and are discussed collectively. Firstly, in several of our simulations (especially those for a bulk salinity of 1 and 5 wt% NaCl) the inclusions trapped at the highest temperatures show somewhat similar volume fractions of vapor between the coeval liquid-rich and vapor-rich inclusions (Fig. 13), and these inclusions could easily be mistaken for critical-density (or "intermediate density") inclusions during petrography—however, during microthermometry, it would be observed that the two inclusion types show different homogenization behavior, with the liquid-rich inclusions homogenizing to the liquid, and the vapor-rich inclusions homogenizing to the vapor phase. As cooling and boiling proceed to lower temperatures, the density of the trapped liquid phase increases progressively, and that of the trapped vapor phase decreases precipitously (Fig. 2B), such that the inclusions trapped form clearly bimodal assemblages of liquid-rich inclusions and inclusions that appear to be filled almost entirely with vapor (Fig. 13). Indeed, we find that vapor-rich inclusions trapped at any temperature less than ~300 °C show vanishingly small volume fractions of liquid, as a result of the very low density of the vapor phase at >300 °C (Fig. 2B). The vapor-rich inclusions shown

on the right hand side of Fig. 13 (those trapped at the lowest temperatures in each simulation) have such low volume fractions of liquid that it cannot even be displayed in the diagram, and inclusions of this type would appear "empty" during petrography, but would be accompanied by liquid-rich inclusions of relatively high density in the same assemblages. We also find that, as a result of a progressive increase in the salinity of the liquid phase during progressive boiling, halite-saturated compositions can be produced by this type of gentle boiling during isenthalpic cooling, but only in the case of a relatively high starting fluid salinity of 15 wt% NaCl. This is contrast to the case for isothermal decompression, which can drive even very low bulk salinities (1 wt% NaCl) toward halite saturation (Fig. 12). This suggests that halite saturation and "boiling to dryness" in most epithermal veins generally requires some degree of forced decompression, for example by tectonic movement, and halite-saturated inclusions are indicative of a process akin to (or preceding) flashing.

# References


Anderson GM (2005) Thermodynamics of Natural Systems, 2nd edn. Cambridge University Press

Bischoff JL, Pitzer KS (1989) Liquid-vapor relations for the system NaCl-H2O: summary of the P-T- x surface from 300° to 500°C. Am J of Sci 289:217-248.

Bodnar RJ, Lecumberri-Sanchez P, Moncada D, Steele-MacInnis M, (2014) Fluid inclusions in hydrothermal ore deposits. In: Heinrich DH, Karl KT (eds) Treatise on Geochemistry, 2nd edn, v. 13. Elsevier, Oxford, pp. 119-142. http://dx.doi.org/10.1016/B978-0-08-095975-7.01105-0

Bodnar RJ, Reynolds TJ, Kuehn CA (1985) Fluid inclusion systematics in epithermal systems. In: Berger BR, Bethke PM (eds) Geology and Geochemistry of Epithermal Systems: Reviews in Economic Geology v. 2. Society of Economic Geologists, Boulder, pp. 73-98.

Brooks HL, Steele-MacInnis M (2019) A model for the solubility of minerals in saline aqueous fluids in the crust and upper mantle. Am J Sci 319:754-787. https://doi.org/10.2475/09.2019.02

Brown KL (1986) Gold deposition from geothermal discharges in New Zealand. Econ Geol 81:979-983. https://doi.org/10.2113/gsecongeo.81.4.979

Buchanan LJ (1981) Precious metal deposits associated with volcanic environments in the Southwest. Arizona Geological Society Digest 14:237–262.

Chambefort I, Stefánsson A (2020) Fluids in Geothermal Systems. Elements 16 (6): 407–411. https://doi.org/10.2138/gselements.16.6.407

Chen X, Zhou Z, Chen Y, Barrier J, Steele-MacInnis M (2022) Fluid boiling during high-grade gold deposition in an epithermal gold-telluride deposit, Guilaizhuang, China. J Geochem Explor (in press).

Cline JS, Bodnar RJ, Rimstidt JD (1992) Numerical simulation of fluid flow and silica transport and deposition in boiling hydrothermal solutions: application to epithermal gold deposits. J Geophys Res 97:9085-9103. https://doi.org/10.1029/91JB03129

Creaser EC, Steele-MacInnis M, Tutolo B (2022) A model for the solubility of anhydrite in $H_2O$-NaCl fluids from 25 to 800 °C, 0.1 to 1400 MPa, and 0 to 60 wt% NaCl: Applications to hydrothermal ore-forming systems. Chem Geol 587:120609. https://doi.org/10.1016/j.chemgeo.2021.120609

Dong G, Morrison G, Jaireth S (1995) Quartz textures in epithermal veins, Queensland - classification, origin, and implication. Econ Geol 90:1842-1856. 10.2113/gsecongeo.90.6.1841

Driesner T, Heinrich CA (2007) The system $H_2O$–NaCl. Part I: Correlation formulae for phase relations in temperature–pressure–composition space from 0 to 1000°C, 0 to 5000 bar, and 0 to 1 $X_{NaCl}$. Geochim Cosmochim Acta 71:4880-4901. 10.1016/j.gca.2006.01.033

Driesner T (2007) The system $H_2O$–NaCl. Part II: Correlations for molar volume, enthalpy, and isobaric heat capacity from 0 to 1000 °C, 1 to 5000 bar, and 0 to 1 $X_{NaCl}$. Geochim Cosmochim Acta 71: 4902–4919. https://doi.org/10.1016/j.gca.2007.05.026

Fournier RO (1985) The behavior of silica in hydrothermal solutions. In: Berger BR, Bethke PM (eds) Geology and Geochemistry of Epithermal Systems: Reviews in Economic Geology v. 2. Society of Economic Geologists, Boulder, pp. 45–61.

Gemmell JB, Simmons SF (2007) A group of papers devoted to epithermal Au Ag deposits. Econ Geol 102:783–1009.

Hedenquist JW, Arribas AR (2022) Exploration implications of multiple formation environments of advanced argillic minerals. Econ Geol 117(3): 609-643. https://doi.org/10.5382/econgeo.4880

Hedenquist JW, Lowenstern JB (1994) The role of magmas in the formation of hydrothermal ore deposits. Nature 370:519-527. http://dx.doi.org/10.1038/370519a0

Hedenquist JW, Arribas AR, Aoki M (2017). Zonation of sulfate and sulfide minerals and isotopic composition in the Far Southeast Porphyry and Lepanto Epithermal Cu–Au Deposits, Philippines. Resource Geol 67:174-196. https://doi.org/ 10.1111/rge.12127

Hedenquist JW, Arribas RA, Gonzalez-Urien E (2000) Exploration for epithermal gold deposits. Gold in 2000, Steffen G. Hagemann, Philip E. Brown https://doi.org/10.5382/Rev.13.07

Henley RW, Brown KL (1985) A practical guide to the thermodynamics of geothermal fluids and hydrothermal ore deposits. In: Berger BR, Bethke PM (eds) Geology and Geochemistry of Epithermal Systems: Reviews in Economic Geology v. 2. Society of Economic Geologists, Boulder, pp. 25–44.

Henley RW, Hughes GO (2000) Underground fumaroles: excess heat effects in vein formation. Econ Geol 95:453-466. https://doi.org/10.2113/gsecongeo.95.3.453

Henley RW, Truesdell AH, Barton Jr. PB, and Whitney JA (1984) Fluid–Mineral Equilibria in Hydrothermal Systems. Society of Economic Geologists, 1. https://doi.org/10.5382/Rev.01

Jensen EP, Barton MD (2000) Gold Deposits related to Alkaline Magmatism. Gold in 2000, Society of Economic Geologists, v.13 https://doi.org/10.5382/Rev.13.08

Klimentyeva D, Driesner T, von Quadt A, Tončic T, Heinrich C (2021) Silicate-replacive high sulfidation massive sulfide orebodies in a porphyry Cu-Au system: Bor, Serbia. Mineralium Deposita 56:1423-1448. https://doi.org/10.1007/s00126-020-01023-2

Klyukin YI, Driesner T, Steele-MacInnis M, Bodnar RJ (2016) Effect of salinity on mass and energy transport by hydrothermal fluids in the critical region based on the physical and

thermodynamic properties of $H_2O$-NaCl. Geofluids 16:585-603. http://dx.doi.org/10.1111/gfl.12181

Klyukin YI, Haroldson EL, Steele-MacInnis M (2020) A comprehensive numerical model for the thermodynamic and transport properties of H2O-NaCl fluids. Chem Geol 557:119840. http://dx.doi.org/10.1016/j.chemgeo.2020.119840

Klyukin YI, Lecumberri-Sanchez P, Steele-MacInnis M, Bodnar RJ (2019) Fluid inclusion phase ratios, compositions and densities, from ambient temperature to homogenization, based on *PVTX* properties of $H_2O$-NaCl. Earth-Sci Rev 198:102924. https://doi.org/10.1016/j.earscirev.2019.102924

Kodera P, Lexa J, Rankin AH, Fallick AE (2005) Epithermal gold veins in a caldera setting: Banska Hodrusa, Slovakia. Mineral Deposita 39:921-943. https://doi.org/10.1007/s00126-004-0449-5

Mavrogenes J, Henley RW, Reyes AG, Berger B (2010) Sulfosalt Melts: Evidence of high-temperature vapor transport of metals in the formation of high-sulfidation lode gold deposits. Econ Geol 105(2):257-262. https://doi.org/10.2113/gsecongeo.105.2.257

Monecke T, Monecke J, Reynolds TJ, Tsuruoka S, Bennett MM, Skewes WB, Palin RM (2018) Quartz solubility in the $H_2O$-NaCl system; a framework for understanding vein formation in porphyry copper deposits. Econ Geol 113:1007-1046. https://doi.org/10.5382/econgeo.2018.4580

Roedder, E (1984) Fluid Inclusions. Reviews in Mineralogy, v. 12

Sander MV, Black JE (1988) Crystallization and recrystallization of growth-zoned vein quartz crystals from epithermal systems; implications for fluid inclusion studies. Econ Geol 83:1052-1060. https://doi.org/10.2113/gsecongeo.83.5.1052

Scott SW, Driesner T, Weiss P (2015) Geologic controls on supercritical geothermal resources above magmatic intrusions. Nature Communications 6:7837. https://doi.org/10.1038/ncomms8837

Simmons SF, Browne PRL (2000) Hydrothermal minerals and precious metals in the Broadlands-Ohaaki geothermal system: Implications for understanding low-sulfidation epithermal environments. Econ Geol 95:971-999. https://doi.org/10.2113/95.5.971

Simmons SF, Browne, (1997) Saline fluid inclusions in sphalerite from the Broadlands-Ohaaki geothermal system; a coincidental trapping of fluids being boiled toward dryness. Econ Geol 92(4): 485-489. https://doi.org/10.2113/gsecongeo.92.4.485

Simmons SF, Christenson BW (1994) Origins of calcite in boiling geothermal systems. Am J Sci 294:361-400. https://doi.org/10.2475/ajs.294.3.361

Steele-MacInnis M, Han L, Lowell RP, Rimstidt JD, Bodnar RJ (2012a) Quartz precipitation and fluid-inclusion characteristics in sub-seafloor hydrothermal systems associated with volcanogenic massive sulfide deposits. Central Eur J Geosci 4:275-286. http://dx.doi.org/10.2478/s13533-011-0053-z

Steele-MacInnis M, Han L, Lowell RP, Rimstidt JD, Bodnar RJ (2012b) The role of fluid phase immiscibility in quartz dissolution and precipitation in sub-seafloor hydrothermal systems. Earth Planet Sci Lett 321-322:139–151. https://doi.org/10.1016/j.epsl.2011.12.037

Steele-MacInnis M, Lecumberri-Sanchez P, Marshall D, Kontak D (2021) Contribution of fluid inclusions to genetic models for ore deposits. In: Lecumberri-Sanchez P, Steele-MacInnis M, Kontak D (eds) Fluid and Melt Inclusions: Applications to Geologic Processes. Topics in Mineral Sciences v. 49, Mineralogical Association of Canada, Ottawa, pp. 195-242.

Steele-MacInnis M, Manning CE (2020) Hydrothermal properties of geologic fluids. Elements 16:375-380. https://doi.org/10.2138/gselements.16.6.375

Vikre PG (1985) Precious metal vein systems in the National District, Humboldt County, Nevada. Economic Geology. 80:360–393. https://doi.org/10.2113/gsecongeo.80.2.360

Wagner W, Pruß A (2002) The IAPWS formulation 1995 for the thermodynamic properties of ordinary water substance for general and scientific use. J Phys Chem Ref Data 31:387-535. http://dx.doi.org/10.1063/1.1461829

White NC, Hedenquist JW (1995) Epithermal Gold Deposits: Styles, Characteristics and Exploration. Society of Economic Geologists, Newsletter. 23: 9-13. http://dx.doi.org/10.5382/SEGnews.1995-23.fea

Weatherley, DK, Henley, RW, (2013) Flash vaporization during earthquakes evidenced by gold deposits. Nature Geoscience, v. 6. 294–298. https://doi.org/10.1038/ngeo1759

Zeeck LR, Monecke T, Reynolds TJ, Tharalson ER, Pfaff K, Kelly NM, Hennigh QT (2021) Textural characteristics of barren and mineralized colloform quartz bands at the low-sulfidation epithermal deposits of the Omu Camp in Hokkaido, Japan: implications for processes resulting in bonanza-grade precious metal enrichment. Econ Geol 116:407-425. https://doi.org/10.5382/econgeo.4795

# Appendix

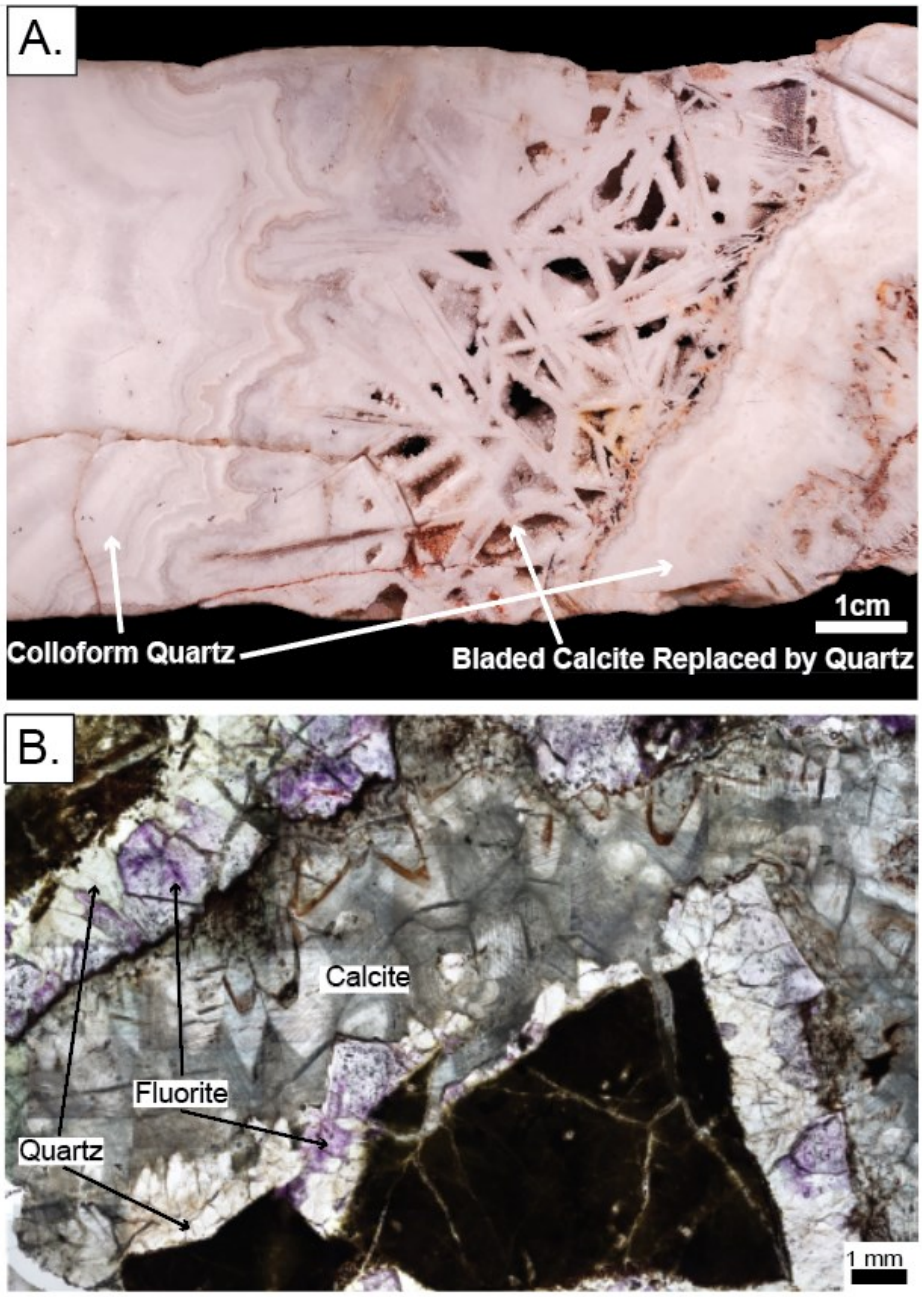


**Figure 1.** Epithermal vein samples showing some common mineral assemblages and textures. A) A typical low-sulfidation vein in which early colloform-textured quartz gives way to bladed calcite that has been replaced by quartz (La Luz vein, Guanajuato, Mexico). B) A typical vein (breccia fill) from an epithermal Au-Te system associated with alkalic magmatism, showing early, feathery-textured quartz that gives way to fluorite, then late calcite, with all three minerals showing open-space filling textures (Guilaizhuang deposit, China; modified from Chen et al., 2022).

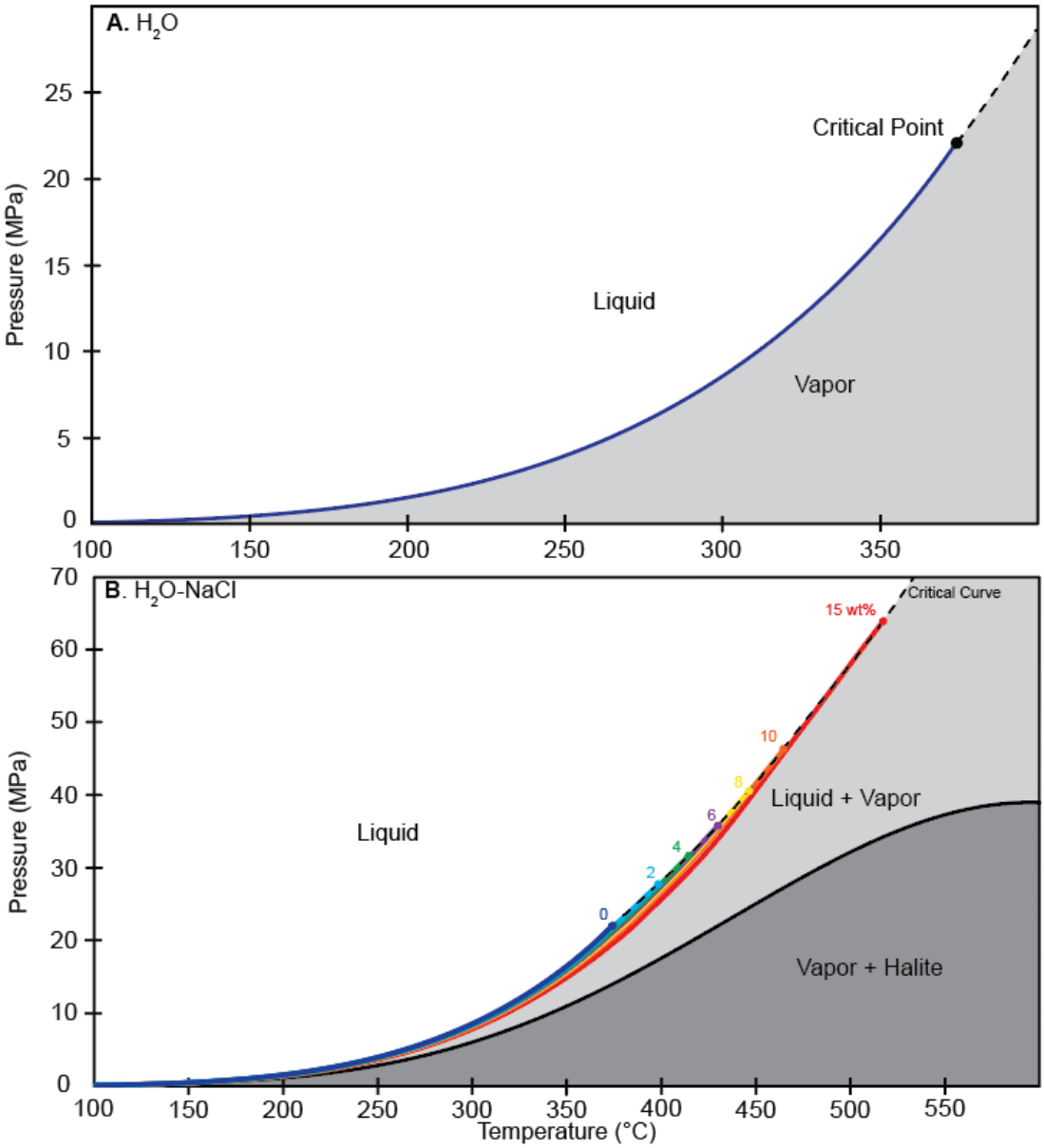


**Figure 2.** A) Phase diagram for the system $H_2O$ showing the liquid-vapor (boiling) curve that terminates at the critical point at 374 °C and 22 MPa. B) Phase diagram for the system $H_2O$-NaCl showing the critical curve (dashed line), the liquid-vapor curves (bubble-point curves) for fluids of salinities ranging from 0 to 15 wt% NaCl (colored lines), and the liquid-vapor-halite curve. Notice that the respective critical points for each salinity lie at the intersection of the liquid-vapor (bubble-point) curve with the critical curve.

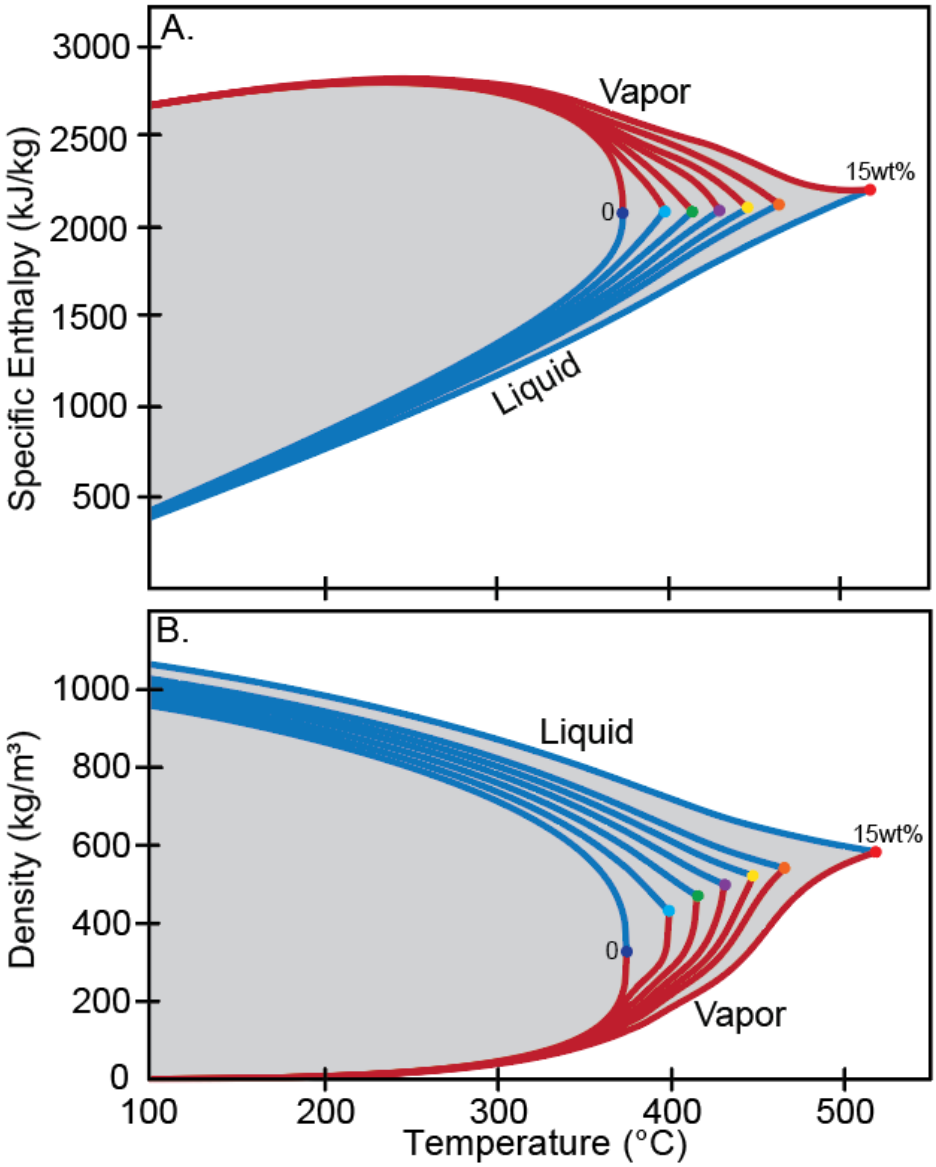


**Figure 3.** Specific enthalpy (A) and density (B) of immiscible liquid and vapor along the respective boiling curves. For each pair of curves, the listed salinity represents the (fixed, constant) salinity of the liquid phase, whereas the salinity of the vapor phase is a sliding variable defined by the phase equilibria and ranging from essentially zero at 100 °C to the same value as that of the liquid at the critical point. Notice that both specific enthalpy and density values of the liquid and vapor converge to become exactly equal at each critical point.

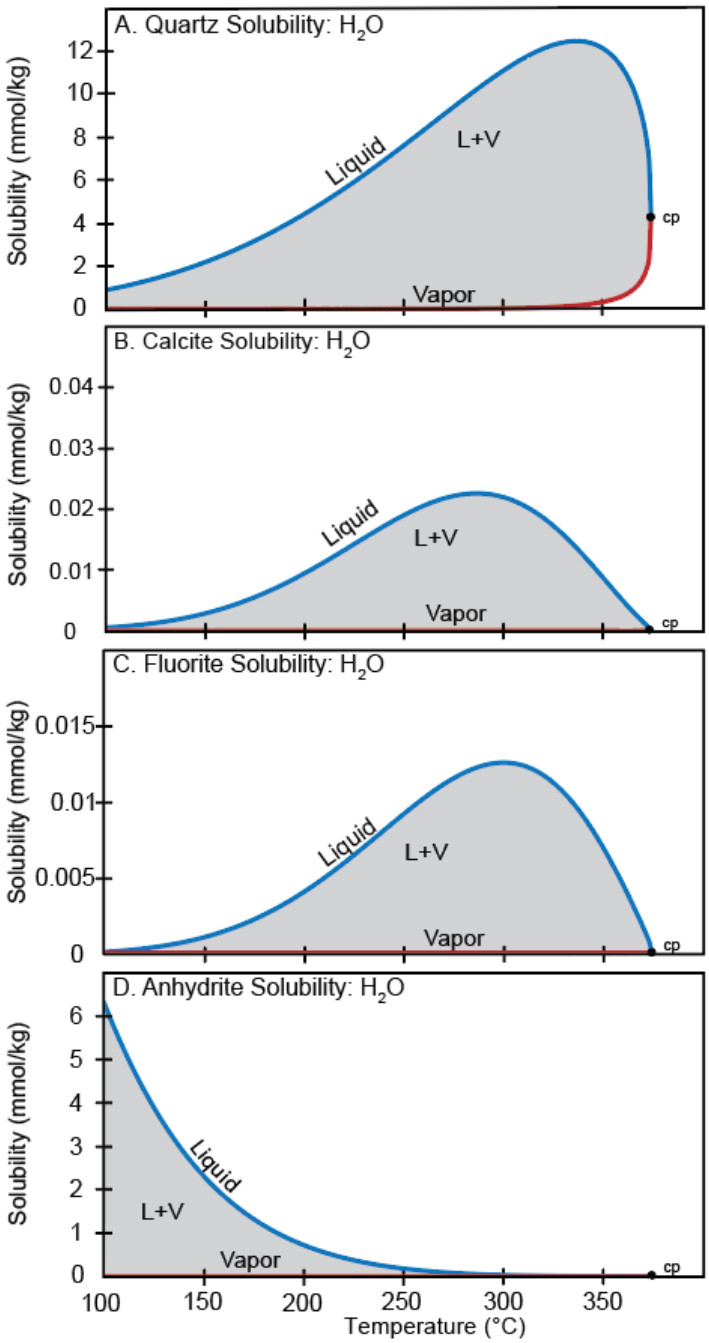


**Figure 4.** Solubilities of quartz (A), calcite (B), fluorite (C) and anhydrite (D) in both liquid and vapor along the boiling curve for an $H_2O$ fluid of 0 wt% NaCl. L+V = liquid plus vapor.

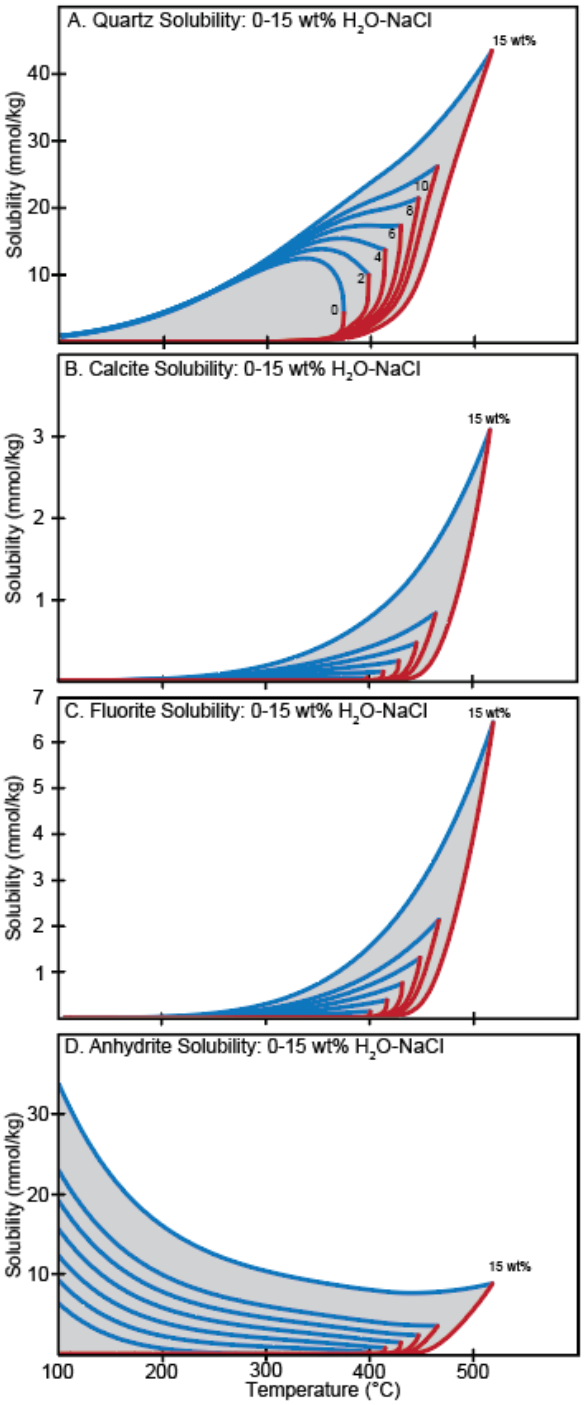


**Figure 5.** Solubilities of quartz (A), calcite (B), fluorite (C), and anhydrite (D) in both the liquid and vapor phase along boiling curves for fluids with salinities of 0 to 15wt% NaCl (increments are 0, 2, 4, 6, 8, 10 and 15 wt%).

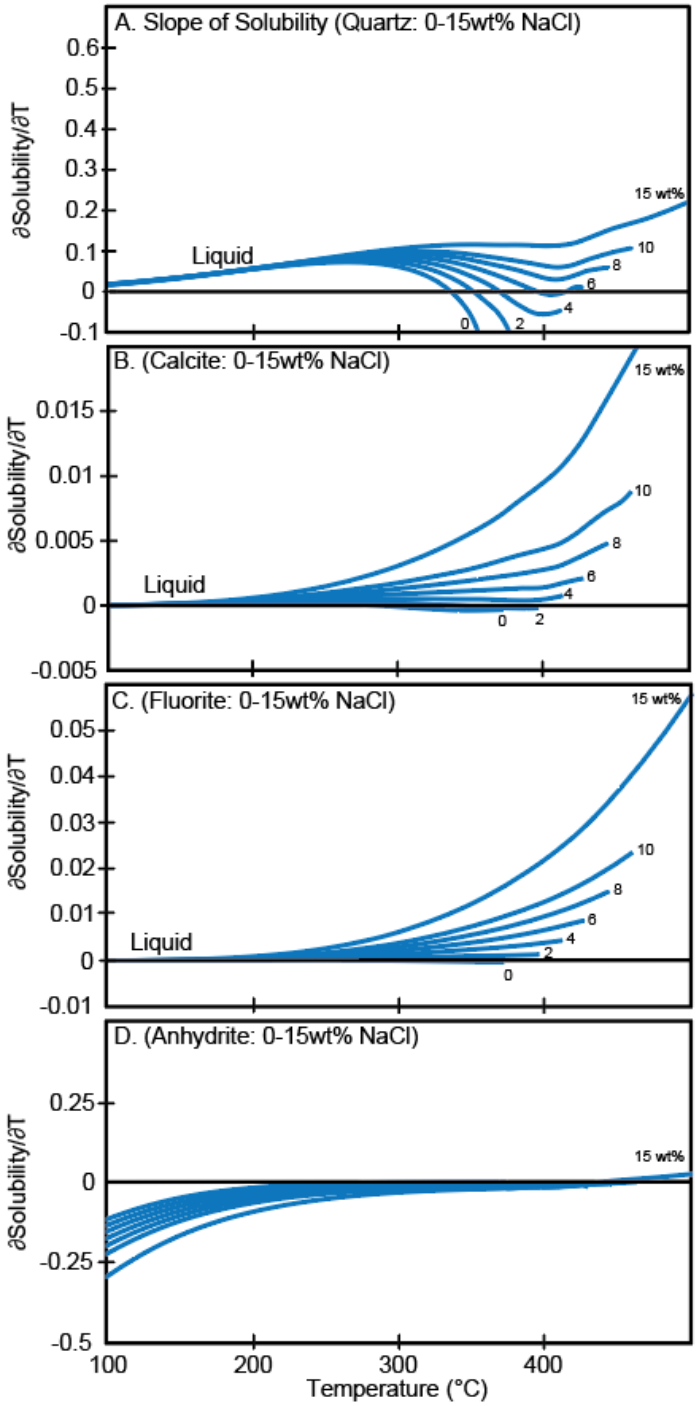


**Figure 6.** Slopes of the solubilities in the liquid phase along the boiling curve for quartz (A), calcite (B), fluorite (C), and anhydrite (D) for the same salinities as shown in Fig. 5. A positive slope indicates prograde solubility (increasing with increasing temperature), whereas a negative slope indicates retrograde solubility (decreasing with increasing temperature).

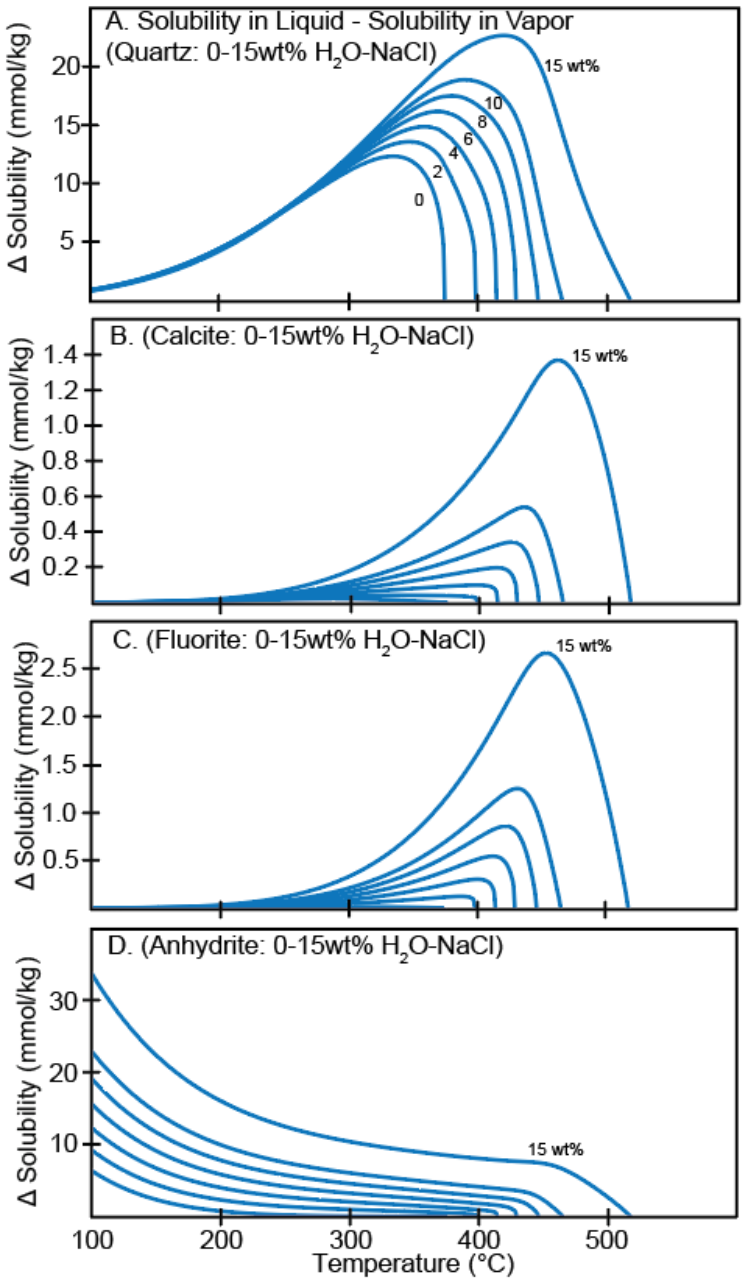


**Figure 7.** Difference in solubility of quartz (A), calcite (B), fluorite (C), and anhydrite (D) between liquid and vapor phase along the boiling curve for the same salinities as shown in Fig. 5.

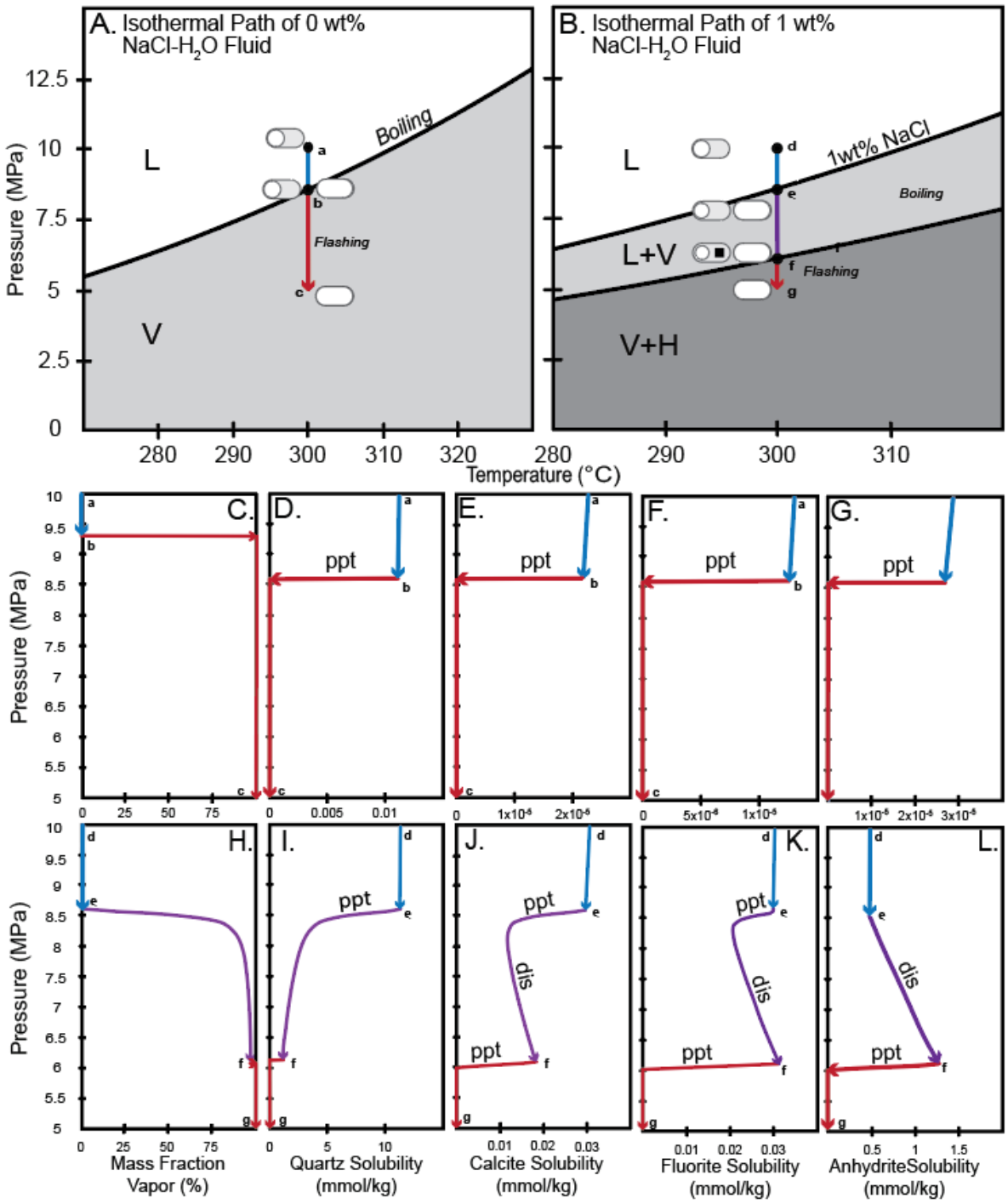


**Figure 8.** Simulations of isothermal decompression for a fluid of pure $H_2O$ (A, C-G) and a 1wt% NaCl-$H_2O$ fluid (B, H-L) from 10 MPa to 5 MPa at 300°C. Upper panels A and B show the pathway in pressure-temperature space; lower panels C and H show the mass fraction of vapor; while panels D-G and I-L illustrate the changes in bulk (total) solubility of quartz, calcite, fluorite and anhydrite. ppt = precipitation (solubility decreasing) and dis = dissolution (solubility increasing). In panels A and B, sketches of fluid inclusions shown at different points represent the room-temperature phase ratios of inclusions that would be predicted to be trapped at specific points along each path, and are shown in more detail in Fig. 12. L = liquid, V = vapor, H = halite.

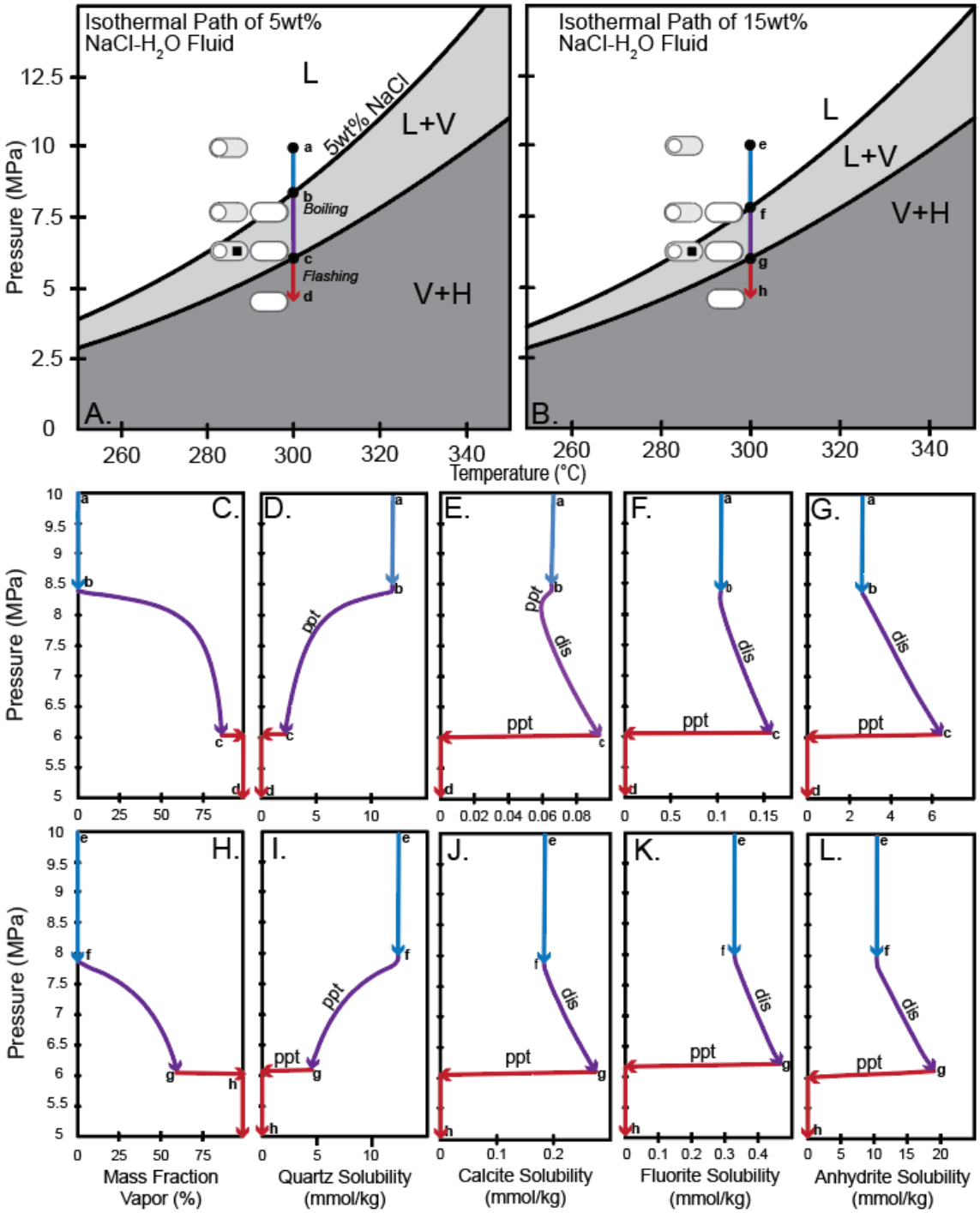


**Figure 9.** Simulations of isothermal decompression for fluids of 5 wt% NaCl (A, C-G) and 15 wt% NaCl (B, H-L) from 10 MPa to 5 MPa at 300°C. Upper panels A and B show the pathway in pressure-temperature space; lower panels C and H show the mass fraction of vapor; while panels D-G and I-L illustrate the changes in bulk (total) solubility of quartz, calcite, fluorite and anhydrite. ppt = precipitation (solubility decreasing) and dis = dissolution (solubility increasing). In panels A and B, sketches of fluid inclusions shown at different points represent the room-temperature phase ratios of inclusions that would be predicted to be trapped at specific points along each path, and are shown in more detail in Fig. 12. L = liquid, V = vapor, H = halite.

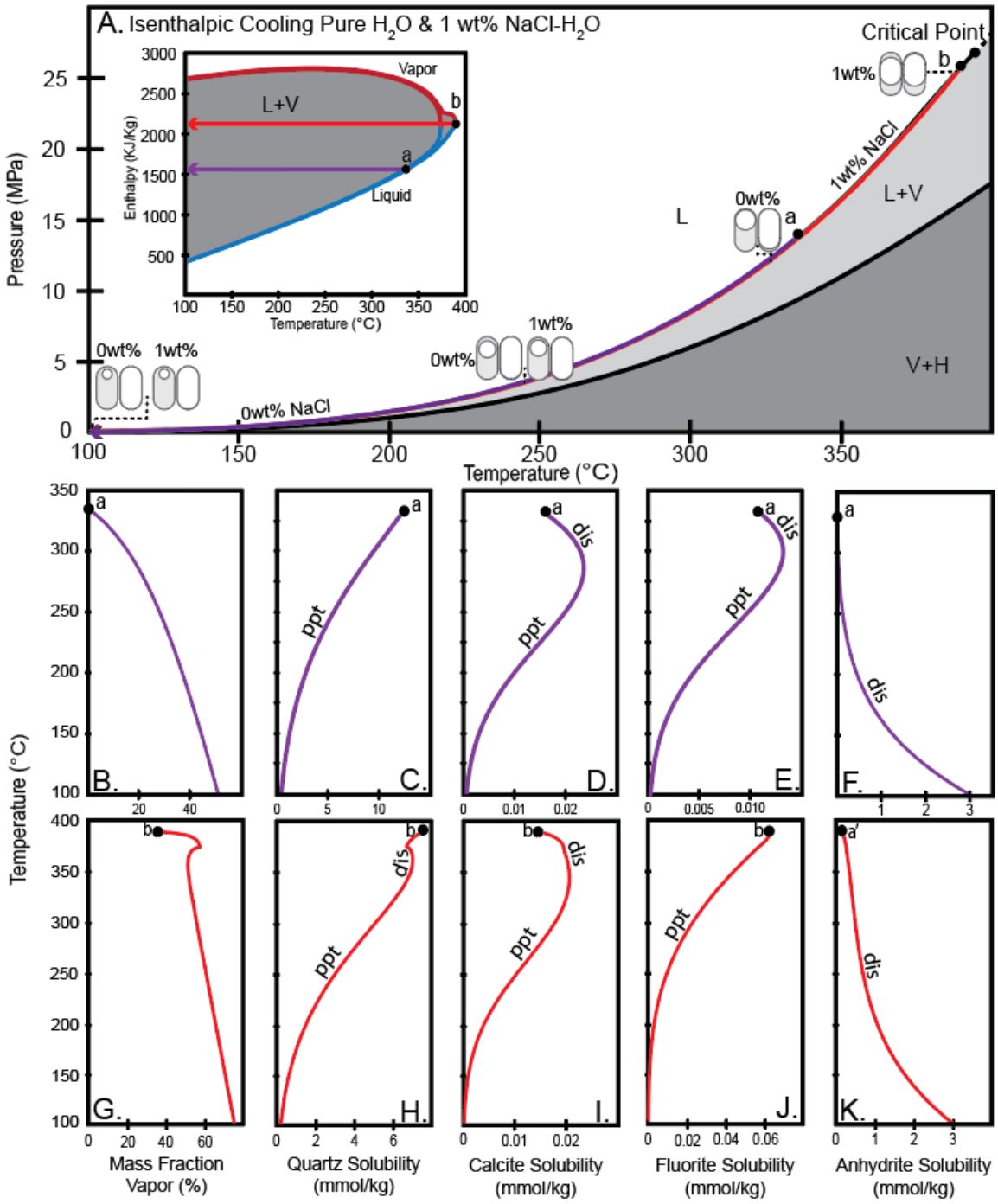


**Figure 10.** Simulations of gentle boiling along an isenthalpic cooling path for a fluid of pure $H_2O$ (pathway starting at point **a**, panels A-F) and a 1 wt% NaCl fluid (pathway starting at point **b**, panels A, G-K). Panel A illustrates the paths in pressure-temperature space and the inset shows the same paths in enthalpy-temperature space. Panels B-K illustrate the variations in mass fraction of vapor (B, G) and solubility of the four minerals (C-F and H-K) as temperature decreases. ppt = precipitation (solubility decreasing) and dis = dissolution (solubility increasing). In panel A, sketches of fluid inclusions shown at different points represent the room-temperature phase ratios of inclusions that would be predicted to be trapped at specific points along each path, and are shown in more detail in Fig. 13. L = liquid, V = vapor, H = halite.

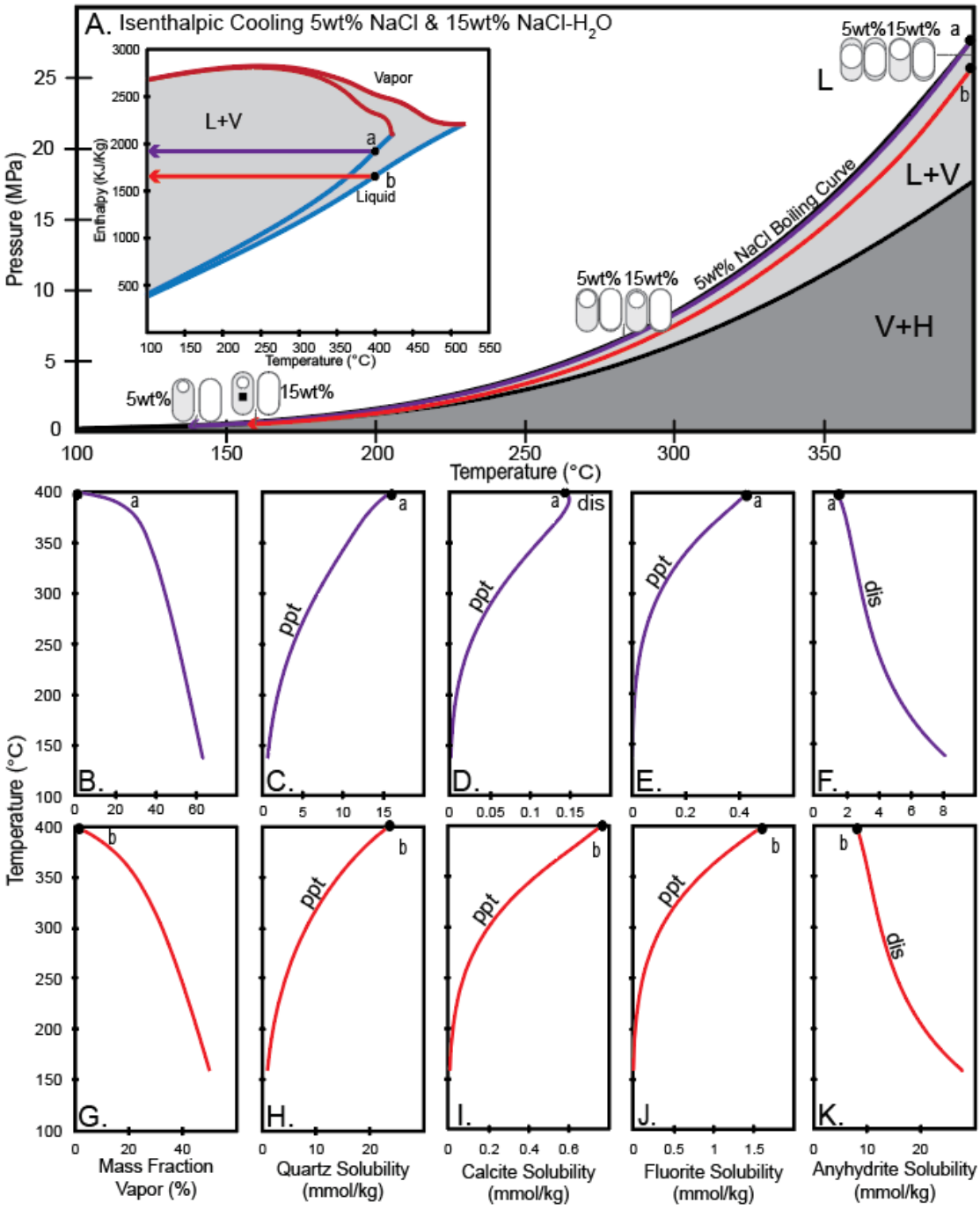


**Figure 11.** Simulations of gentle boiling along an isenthalpic cooling path for fluids of 5 wt% NaCl (pathway starting at point **a**, panels A-F) and 15 wt% NaCl fluid (pathway starting at point **b**, panels A, G-K). Panel A illustrates the paths in pressure-temperature space and the inset shows the same paths in enthalpy-temperature space. Panels B-K illustrate the variations in mass fraction of vapor (B, G) and solubility of the four minerals (C-F and H-K) as temperature decreases. ppt = precipitation (solubility decreasing) and dis = dissolution (solubility increasing). In panel A, sketches of fluid inclusions shown at different points represent the room-temperature phase ratios of inclusions that would be predicted to be trapped at specific points along each path, and are shown in more detail in Fig. 13. L = liquid, V = vapor, H = halite.

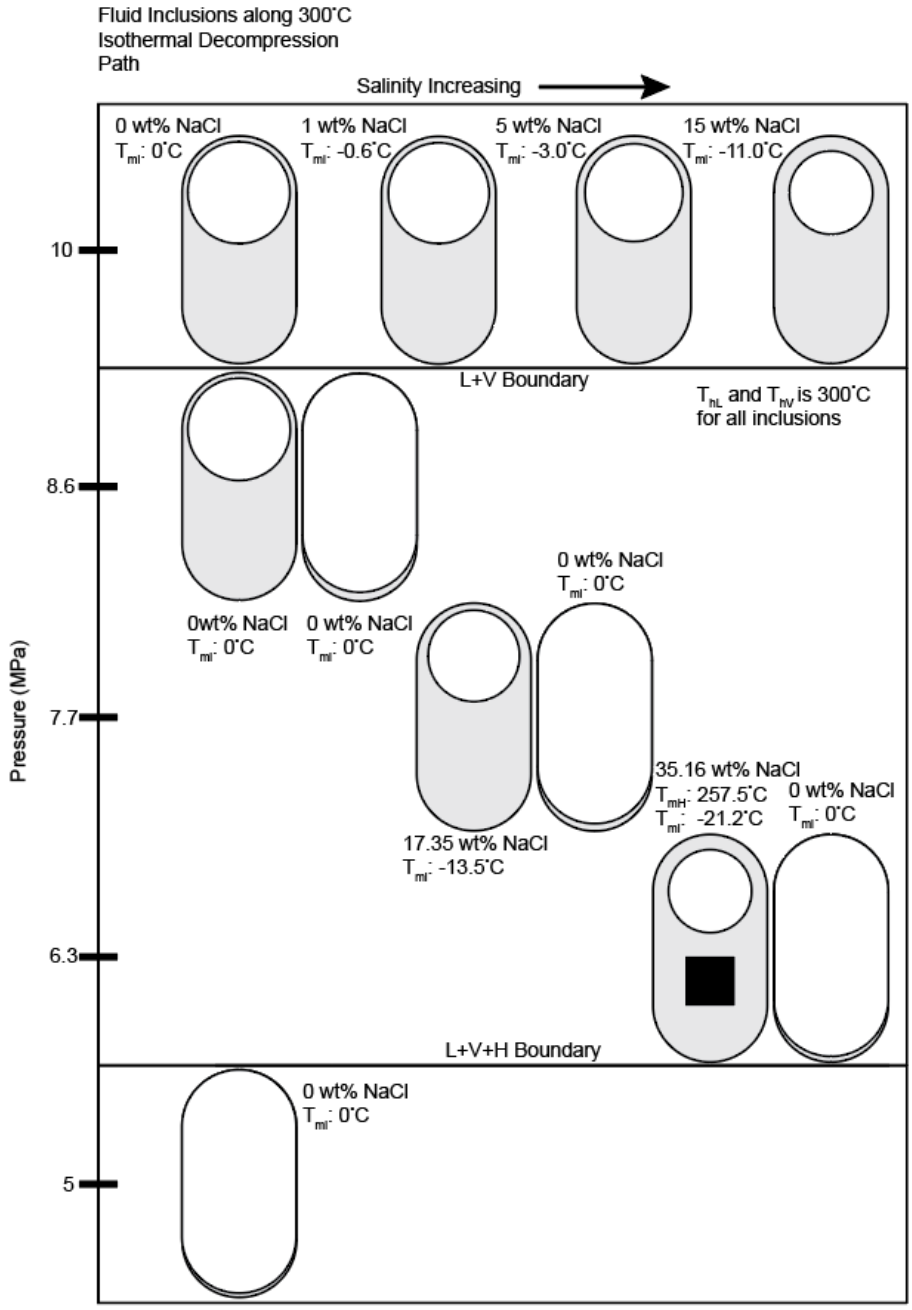


**Figure 12.** Predicted microtherometric properties and volumetric phase ratios at room temperature for fluid inclusions trapped at specific points along the isothermal decompression pathways shown in Figs. 8 and 9. Top panel = liquid-rich inclusions trapped in the single-phase (liquid) field. Middle panel = coeval liquid-rich and vapor-rich inclusions trapped during boiling. Bottom panel = only vapor-rich inclusions trapped at pressures below the liquid-vapor-halite curve. Note: the sketches of the room-temperature phase ratios are quantitative, and are drawn assuming a cylindrical fluid inclusion with hemispherical ends, a spherical vapor bubble (or, if the bubble size exceeds the radius of the inclusion, a cylindrical bubble with hemispherical ends) and a cubic halite grain (see Klyukin et al., 2019). $T_{mi}$ = ice melting temperature; $T_{mH}$ = halite melting temperature; $T_{hL}$ = temperature of homogenization to the liquid phase; $T_{hV}$ = temperature of homogenization to the vapour phase.

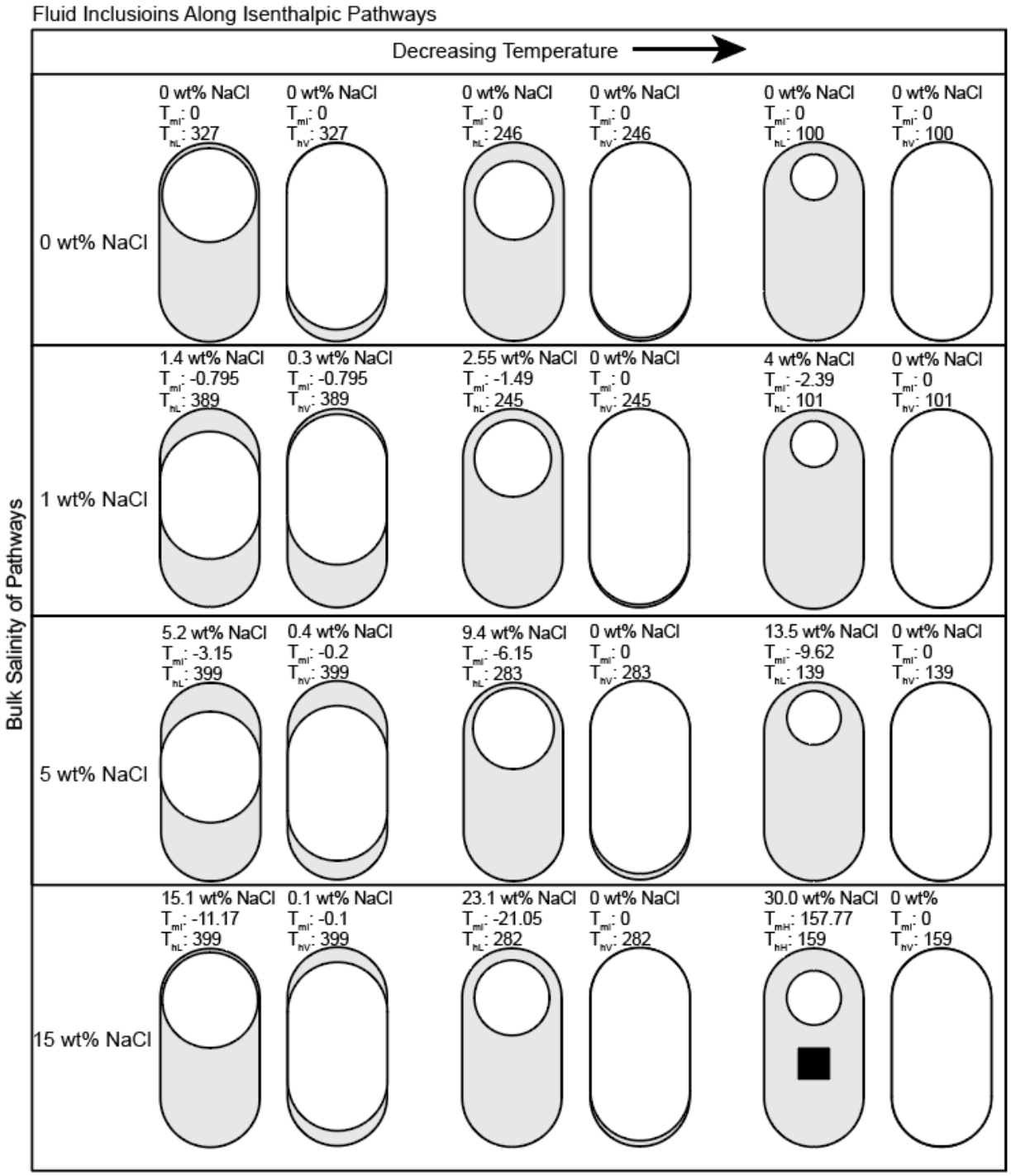


**Figure 13.** Predicted microtherometric properties and volumetric phase ratios at room temperature for fluid inclusions trapped at specific points along the gently boiling, isenthalpic cooling pathways shown in Figs. 10 and 11. Approach to sketching and abbreviations the same as in Fig. 12.